ACS APPLIED MATERIALS & INTERFACES

Research Article

www.acsami.org

Nitrogen-Doped Yolk–Shell-Structured CoSe/C Dodecahedra for High-Performance Sodium Ion Batteries

Yifang Zhang,[†] Anqiang Pan,[*,†] Lin Ding,[†] Zilong Zhou,[‡] Yaping Wang,[†] Shaoyu Niu,[†] Shuquan Liang,[*,†] and Guozhong Cao[*,§]

[†]School of Materials Science & Engineering, Central South University, Changsha 410083, Hunan China

[‡]School of Resources & Safety Engineering, Central South University, Changsha 410083, Hunan China

[§]Department of Materials Science & Engineering, University of Washington, Seattle, Washington 98195, United States

Supporting Information

ABSTRACT: In this work, nitrogen-doped, yolk–shell-structured CoSe/C mesoporous dodecahedra are successfully prepared by using cobalt-based metal–organic frameworks (ZIF-67) as sacrificial templates. The CoSe nanoparticles are in situ produced by reacting the cobalt species in the metal–organic frameworks with selenium (Se) powder, and the organic species are simultaneously converted into nitrogen-doped carbon material in an inert atmosphere at temperatures between 700 and 900 °C for 4 h. For the composite synthesized at 800 °C, the carbon framework has a relatively higher extent of graphitization, with high nitrogen content (17.65%). Furthermore, the CoSe nanoparticles, with a size of around 15 nm, are coherently confined in the mesoporous carbon framework. When evaluated as novel anode materials for sodium ion batteries, the CoSe/C composites exhibit high capacity and superior rate capability. The composite electrode delivers the specific capacities of 597.2 and 361.9 mA h g^{-1} at 0.2 and 16 A g^{-1}, respectively.

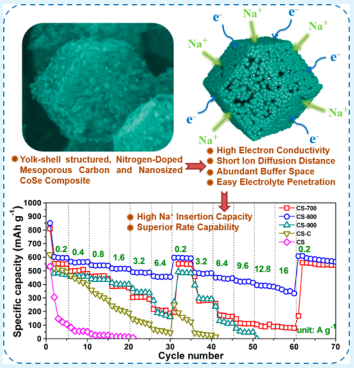

KEYWORDS: *nitrogen-doped carbon, metal–organic frameworks, cobalt selenide, sodium ion batteries, anode*

1. INTRODUCTION

Electrochemical energy storage and conversion systems have attracted tremendous attention due to the energy crisis and environmental issues.[1−3] The electrode materials are one of the major determinants to obtain high-performance energy storage devices. Recently, transition-metal chalcogenides (TMCs) were extensively studied as electrode materials due to their higher lithium/sodium storage capacity, wide availability, and enhanced safety.[4−6] However, the large volume changes upon cycling and the low electron conductivity restrict their applications in high power density devices. To address this issue, hybridization of TMCs with conductive materials is considered a rational solution to improve their electron transportation capability.[7−9] On the other hand, making mesoporous or hollow structures with large surface areas are desired to maximize the electrochemical performance of TMCs.[10−13] Although quite mature explorations have been implemented on the designs of electrode materials, in the scientific field, it is still of great interest to develop novel and facile synthetic strategies to mimic the structural advantages and further improve their electrochemical performances.

Transition-metal selenides have attracted increasing attention in applications for rechargeable batteries, supercapacitors, and catalysts.[14−16] Among them, cobalt selenides in a widely varied composition of CoSe, $CoSe_2$, and $Co_{0.85}Se$ phases exhibit delightful performance in energy storage devices, and many hybrids have been reported. For example, $CoSe_x$–reduced graphene oxide (rGO) composites demonstrate good electrochemical properties for rechargeable batteries.[17,18] Moreover, $CoSe_x$ nanowires or nanowire arrays were grown on carbonaceous substrates, such as carbon fiber paper and carbon cloth, for high-performance supercapacitors.[19,20] However, the fabrication of complex coherent mesoporous $CoSe_x$/C composites and their application in sodium ion batteries are much less reported.

More recently, metal–organic frameworks (MOFs) have been widely studied as an emerging class of crystalline porous materials. MOFs are composed of well-organized metal centers and organic linkers. The organic ligands of some MOFs contain nitrogen species that can be used as raw materials to produce N-doped carbon materials.[21−23] The heteroatom introduces defects within the carbon material that increases the electronic conductivity and creates abundant active sites.[24−26] Moreover, studies have shown the reduction of electrolyte decomposition by nitrogen doping.[27] Moreover, the wide availability of metal–organic frameworks with diversified structures, such as micro-octahedral,[28] dodecahedra,[4,29] nanocages,[30] makes them of advantageous in fabricating active material and carbon composites with multiple shapes.

Herein, we report the novel synthesis of yolk–shell-structured mesoporous CoSe/C dodecahedra using cobalt-based organic frameworks (ZIF-67) as the sacrificial templates.

Received: October 16, 2016
Accepted: January 11, 2017
Published: January 11, 2017

DOI: 10.1021/acsami.6b13153
ACS Appl. Mater. Interfaces 2017, 9, 3624−3633

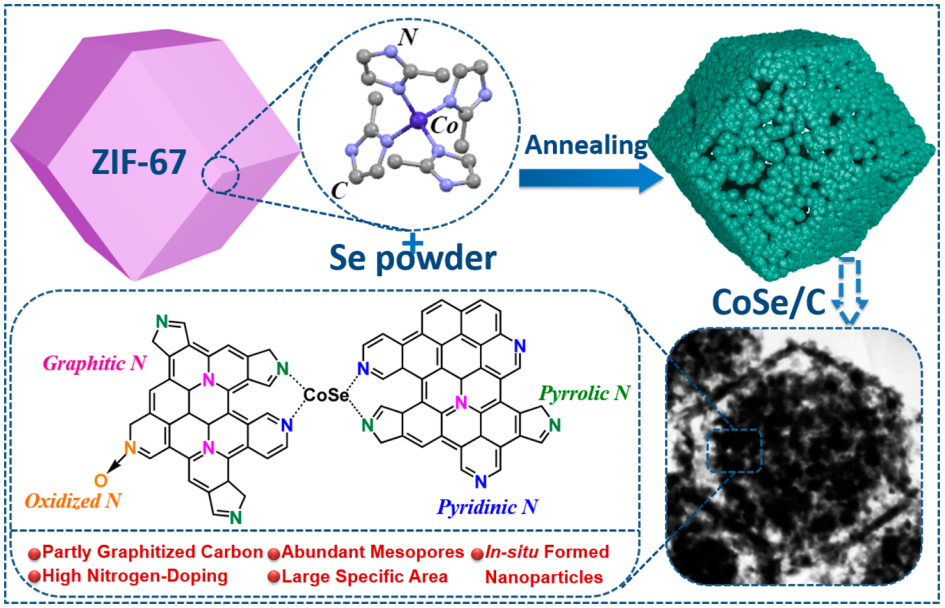

Figure 1. Schematic illustration of the preparation of the nitrogen-doped CoSe/C composites.

The obtained CoSe nanoparticles are coherently surrounded by N-doped carbon frameworks and the obtained composites are of high porosity. The CoSe/C composites exhibit good rate capability and cycling stability as novel anode materials for sodium ion batteries.

2. EXPERIMENTAL SECTION

Synthesis of ZIF-67 Sacrificial Templates. Cobalt nitrate hexahydrate (1.164 g, 4 mmol) and 2-methylimidazole (1.642 g, 20 mmol) were dissolved in 100 mL of methanol separately. The obtained solutions were mixed and incubated at room temperature for 24 h. The resulting precipitates (ZIF-67) were collected by centrifugation, washed with ethanol three times, and then dried for further usage.

Synthesis of CoSe/C Dodecahedra. The above prepared ZIF-67 was mixed with selenium powders in a mass ratio of 1:1 and annealed under Ar atmosphere at 700, 800, or 900 °C for 4 h, and the obtained products were denoted as CS-700, CS-800, and CS-900, respectively. For comparison, CoSe/C composite without nitrogen doping (denoted as CS-C) was also prepared by annealing a mixture of cobalt, selenium powders, and glucose at 800 °C for 4 h under Ar atmosphere. The molar ratio of Co:Se was 1:1 and the mass of glucose was 20% of the total weight of Co and Se powders. Bare CoSe was prepared by a similar process without using glucose and was denoted as CS.

Materials Characterization. The XRD patterns were recorded on a Rigaku D/max 2500 XRD (Cu Kα radiation, λ = 1.541 78 Å). Thermogravimetric analysis (TGA) was conducted on a NETZSCH STA 449C instrument. The morphologies and structures of the samples were characterized by scanning electron microscopy (SEM, Nova NanoSEM230) and transmission electron microscopy (TEM, Titan G2 60-300 with image corrector). X-ray photoelectron spectroscopy (XPS) was performed on an ESCALAB 250Xi (ThermoFisher-VG Scientific). Nitrogen adsorption−desorption measurements were conducted at 77 K (NOVA 4200e, Quantachrome Instruments).

Electrochemical Measurements. The CoSe, CoSe/C, and nitrogen-doped CoSe/C composites were mixed with Super P and sodium carboxymethyl cellulose (CMC) at the weight ratio of 80:10:10 in distilled water to form a slurry, which was coated on copper foil. After vacuum drying at 100 °C for 12 h, the electrodes were assembled into 2025-type coin cells in a glovebox (Mbraun, Garching, Germany) filled with ultra-high-purity argon. The mass loading of the electrode materials on copper foil was about 1 mg cm^{-2}. In the coin cells, Na metal foil and glass microfiber (Whatman, GF/D) were used as the anode and separator, respectively, and 1 M $NaClO_4$ in propylene carbonate (PC) with 5% fluoroethylene carbonate (FEC) was used as the electrolyte. Cyclic voltammetry (CV) was tested with an electrochemical workstation (CHI660C) at a scan rate of 0.1 mV s^{-1} in the voltage range of 0.01−3 V (vs Na/Na$^+$). The galvanostatic charge/discharge performances of the electrodes were conducted at room temperature on a Land battery tester (Land CT 2001A, Wuhan, China). The electrochemical impedance spectroscopy (EIS) was obtained using an AUTOLAB electrochemical station (Metrohm) in the frequency range from 100 kHz to 10 mHz.

3. RESULTS AND DISCUSSION

Figure 1 illustrates the fabrication of N-doped mesoporous CoSe/C composites. The obtained cobalt-based organic frameworks, ZIF-67, are of dodecahedron shape with a size of about 500 nm [Figure S1, Supporting Information (SI)]. Moreover, the XRD pattern of ZIF-67 matches well with the simulated result (Figure S2, SI), demonstrating the successful preparation. The ZIF-67 framework is employed as the sacrificial templates for the preparation of CoSe/C dodecahedra. After annealing ZIF-67 with selenium powder in Ar atmosphere, the Co^{2+} from ZIF-67 reacts with Se powder to in situ produce the CoSe nanoparticles, and the surrounding organic species are converted into a nitrogen-doped carbon framework. Moreover, a mesoporous framework is created during the high-temperature annealing process. The formation of the mesoporous framework may be attributed to the decomposition of organic species and reorganization of atoms to form the new phase of CoSe. Moreover, yolk−shell interiors are created for the CoSe/C composite under the Kirkendall effect between Co and Se species during the annealing process.

The reaction between ZIF-67 and Se powder was first studied by DSC and TG analysis, and the results are shown in Figure 2a. The observation of an endothermic peak at 223.9 °C is due to the melting of selenium powder.[31−33] The detection of a sharp endothermic peak at 298.6 °C and the corresponding drastic mass loss of 25.9% may be attributed to the reaction between ZIF-67 and selenium. To confirm this assumption, a ZIF-67 and Se mixture was annealed at 300 and 600 °C,

DOI: 10.1021/acsami.6b13153
ACS Appl. Mater. Interfaces 2017, 9, 3624−3633

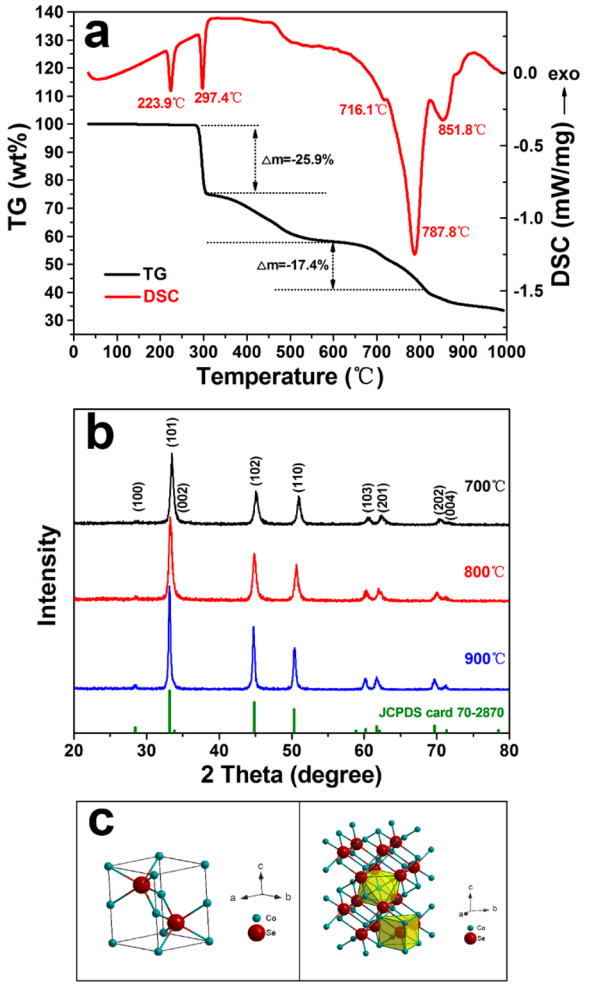

Figure 2. (a) TG and DSC results of the mixture of ZIF-67 and Se powders from room temperature to 1000 °C under the flow of Ar gas, using a temperature ramping rate of 5 °C min^{-1}. (b) XRD patterns of the CoSe/C composite synthesized at different temperatures (700, 800, and 900 °C). (c) Crystal structure of CoSe.

respectively, and the products were characterized by XRD techniques. As shown in Figure S3 (SI), the XRD patterns of both samples can be indexed to orthorhombic $CoSe_2$ [JCPDS Card No. 53-0449: *Pnnm* (No. 58), a = 4.85 Å, b = 5.827 Å, c = 3.628 Å]. The results demonstrate that $CoSe_2$ is first formed at relative low annealing temperatures between cobalt and selenium. However, the CoSe phase starts to appear at 600 °C. The gradual weight loss in this process is due to the further decomposition and carbonization of the organic ligands of ZIF-67 (Figure 2a). The decomposition temperature for pure ZIF-67 is around 600 °C (see Figure S4, SI).[34] Therefore, the chemical bonds between Co and the organic species in ZIF-67 would break down first due to the reaction between Co and Se, and the remaining organic frameworks further decompose at around 600 °C. The small endothermic peak at 716.1 °C may be caused by the evaporation of extra selenium. Meanwhile, the $CoSe_2$ is converted to CoSe.[33] The continuous weight loss is also detected for pure ZIF-67 templates at temperatures higher than 600 °C, which can be attributed to the further carbonization of organic species. Thus, the weight loss after 600 °C on the TG curve (Figure 2a) can be assigned to the combined effect of Se evaporation and further carbonization of organic species. The weight becomes stable when the temperature is higher than 800 °C, implying that the complete carbonization of the organic species needs annealing temperatures higher than 800 °C. Figure 2b shows the identified XRD peaks for all samples, which can be assigned to CoSe [JCPDS Card No. 70−2870: $P6_3/mmc$ (No. 194), a = 3.62 Å, c = 5.286 Å]. With the increase of calcinations temperature, the peak intensity of CoSe becomes stronger, and the full width at half-maximum (fwhm) of the reflection peaks becomes thinner, indicating higher crystallinity. The crystallite size of the samples can be calculated by the Scherer equation (eq 1)

$$D = \frac{k\lambda}{\beta \cos\theta} \quad (1)$$

where D is the size of crystallites; k is the Scherer constant, having the value of 0.9; λ is the wavelength of the X-ray (1.54 Å); and β is the fwhm of the reflection peaks located at angle θ. The calculated crystallite sizes are 15.2, 16.1, and 28.9 nm for CS-700, CS-800, and CS-900, respectively. The average sizes of the crystallite increase with increasing calcination temperature. The crystal structure of CoSe is illustrated in Figure 2c. The CoSe is the hexagonal B81 structure of NiAs. The Se anions are hexagonal close packing (hcp), creating octahedra that share common faces along the c-axis. The Co cations occupy the center site of the octahedra. The Se anions occupy the center site of the triangular prisms created by Co cations.

Figure 3 shows the morphologies of the dodecahedron-shaped CoSe/C composites obtained by annealing ZIF-67 and selenium powder at different temperatures (700, 800, and 900 °C). According to the SEM images, the dodecahedral shape can be well-reserved from ZIF-67 for all the three samples and the dodecahedra are in a narrow size distribution of around 500 nm, quite similar to the ZIF-67 templates. However, a rough surface with different nanoparticle sizes is detected for the dodecahedra. The TEM images give more detailed information about the interior structure of the dodecahedra. Both CS-700 (Figure 3b) and CS-800 (Figure 3d) dodecahedra are made up of nanoparticles with diameters of around 15 nm. However, for CS-900 (Figure 3e,f), the particles become much larger, with diameters of around 40 nm, which can be assigned to the growth of CoSe particles at high temperatures. The results correspond well with the crystallite sizes calculated by XRD results. It is worth mentioning that the dodecahedra are yolk−shell structured with a small interspace between the dodecahedral shell and the spherical yolk. The formation of a yolk-structured interior can be explained by the diffusion-controlled process or Kirkendall effects. Owing to the abundant selenium around the ZIF-67 templates and the high surface energy, the reaction between Se and Co is much faster on the exterior surface of the dodecahedra than in the interior.[35] The outward diffusion of cobalt in the ZIF-67 to react with selenium is faster than the inward diffusion of Se. The difference of diffusion flux can create a gap between the exterior shell and yolk core, forming the yolk−shell structure. Figure 3g clearly shows the mesoporous structure of the CS-800 dodecahedra and the ample space between the interconnected CoSe nanoparticles. The HRTEM image in Figure 3h displays the observed fringe spacing of 2.64 and 2.69 Å, which correspond to the planar distances of (002) and (101) of CoSe, respectively. Moreover, the nanoparticles are covered by a carbon layer, which can facilitate the electronic transportation. The elemental mapping results (Figure 3i) tested by HAADF technique demonstrate the homogeneous distribution of Co, Se, C, and N elements throughout the dodecahedra. To

DOI: 10.1021/acsami.6b13153
ACS Appl. Mater. Interfaces 2017, 9, 3624−3633

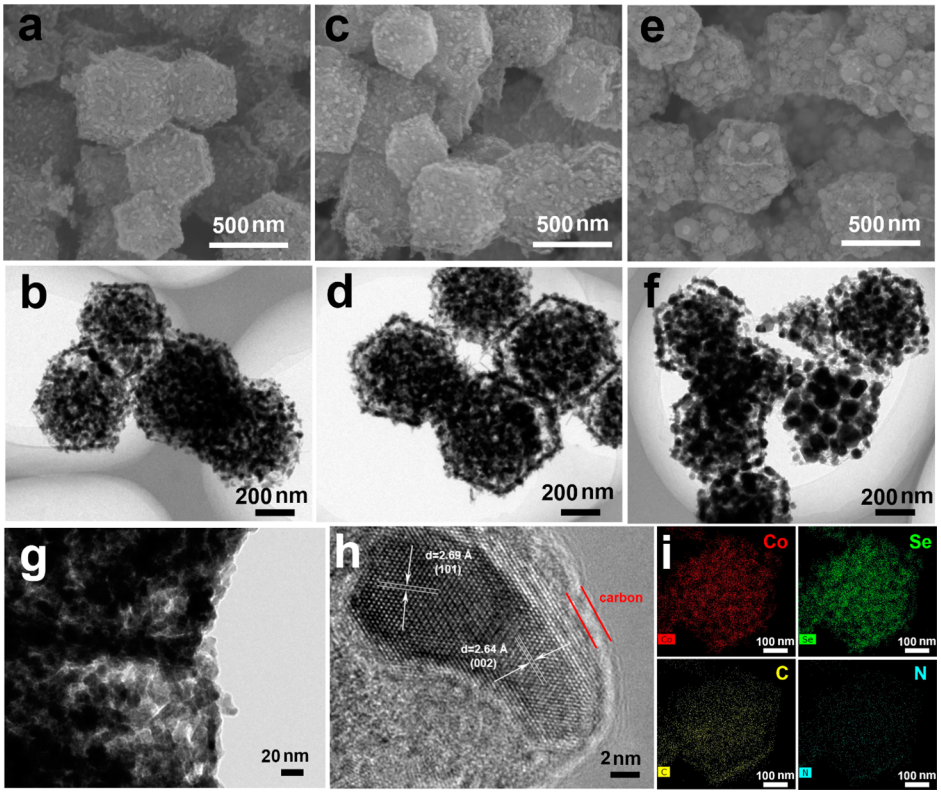

Figure 3. SEM and TEM images of the CoSe/C composites synthesized at different temperatures: (a, b) CS-700, (c, d) CS-800, (e, f) CS-900. The high-magnification TEM images (g, h), and (i) elemental mapping images (Co, Se, C, and N) of CS-800.

Table 1. Percentages of Carbon in the Composites, Nitrogen Content in the Carbon Framework, and Different Types of N in the Nitrogen-Doped CoSe/C Composites

			% of total N 1s			
sample	carbon in the composites (wt %)	nitrogen in carbon (wt %)	pyridinic N	pyrrolic N	graphitic N	oxidized N
CS-700	17.19	24.66	32.59	29.20	24.54	13.67
CS-800	12.21	17.65	25.99	27.32	28.21	18.48
CS-900	11.18	7.95	18.96	21.81	31.62	27.61

estimate the ratio of CoSe in the composites, TG analyses were conducted under air atmosphere with a heating rate of 10 °C min^{-1} (Figure S5, SI). During the heating process, the composites may undergo oxidation of cobalt and selenium species, sublimation of selenium oxide,[33] and combustion of carbon. On the basis of the final product Co_3O_4 (XRD patterns in Figure S6, SI), the weight percentages of carbon in the composite are 17.19%, 12.21%, and 11.18% for CS-700, CS-800, and CS-900, respectively (Table 1). In general, the carbon graphitization degree increases with higher temperature. The carbon contents for CS-800 and CS-900 are almost the same, implying the thorough carbonization of the organic species at temperatures higher than 800 °C.

The chemical compositions of the nitrogen-doped CoSe/C composites were further investigated by X-ray photoelectron spectroscopy (XPS). The survey spectra shown in Figure 4a indicate the presence of Co, Se, C, and N elements in the composite. The existence of N element can be verified by the N 1s spectra in Figure 4b–d. The spectra show the different oxidation states of nitrogen atoms, including pyridinic N, pyrrolic N, graphitic N, and oxidized N at binding energies of 398.3 ± 0.2, 399.1 ± 0.1, 400.8 ± 0.2, and 402.4 ± 0.2 eV, respectively.[36] The C 1s spectra in Figure S7a–c (SI) display peaks at 284.6 ± 0.1, 285.6 ± 0.1, and 287.5 ± 0.2 eV, which can be attributed to the sp^2 C, N–sp^2 C, and N–sp^3 C bonds,[37] respectively, indicating the successful nitrogen doping of the carbon. According to the relative atomic ratio of C and N, the N contents in the carbon frameworks for the three samples are calculated and listed in Table 1. The N content decreases with the increase of pyrolysis temperature. The nitrogen content in the carbon framework is 17.65% for CS-800, which is much higher than those of previously reported nitrogen-doped carbon materials.[38−40] Table 1 also summarizes the fitting results for the N 1s spectra. As the temperature increases, the contents of pyridinic N and pyrrolic N decrease, while those of graphitic N and oxidized N increase. The doped nitrogen can improve the electronic conductivity of carbon. In particular, pyridinic N and pyrrolic N are more favorable because they can create numerous extrinsic defects and active sites.[25,41] The contents of pyridinic N and pyrrolic N are much higher for both CS-700 and CS-800 samples, which benefit the conductivity of the carbon frameworks.

Figure 5 shows the nitrogen adsorption–desorption isotherm curves and pore size distribution of the nitrogen-doped CoSe/C composites. In Figure 5a–c, all adsorption–desorption isotherm curves display type IV isotherms with type H3

DOI: 10.1021/acsami.6b13153
ACS Appl. Mater. Interfaces 2017, 9, 3624–3633

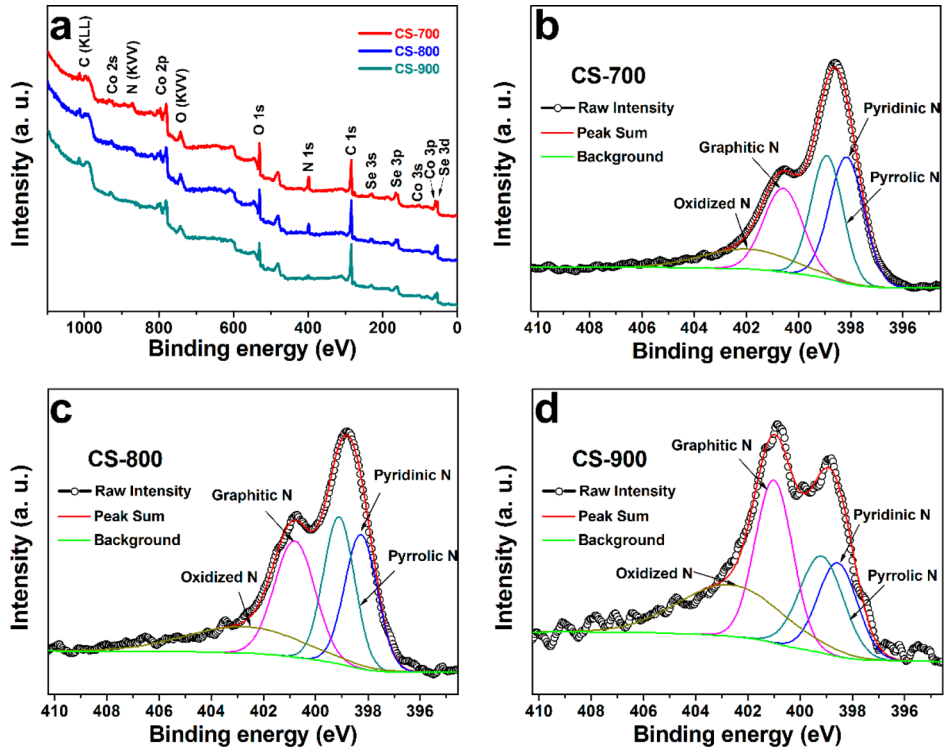

Figure 4. XPS survey spectra (a) and high-resolution XPS spectra of N 1s (b–d) of the CoSe/C composites of (CS-700, CS-800, and CS-900).

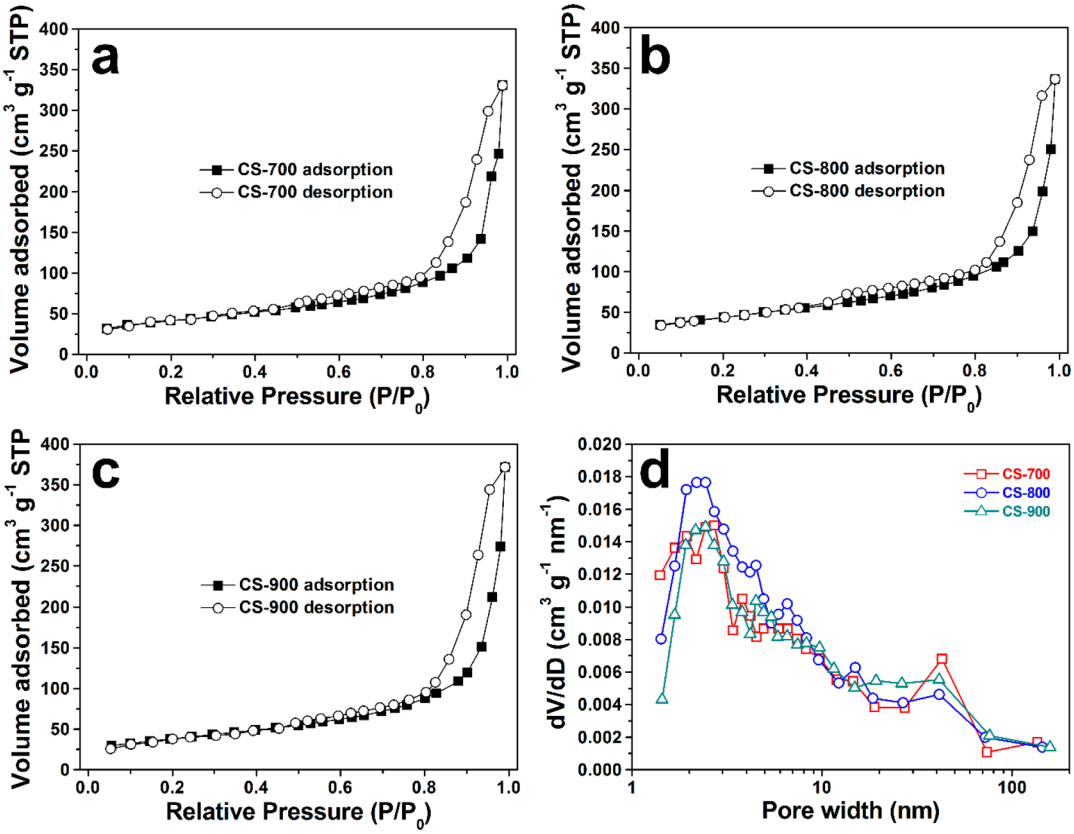

Figure 5. Nitrogen adsorption–desorption isotherms of CS-700 (a), CS-800 (b), and CS-900 (c) and their pore size distribution profiles (d).

hysteresis loops in the relative pressure range of 0.5–1.0 p/p_0, indicating the mesoporous structure of the samples.[42] According to the Brunauer–Emmett–Teller (BET) method, the hollow structures possess large surface areas of 143.4, 154.2, and 134.5 $m^2\ g^{-1}$ for CS-700, CS-800, and CS-900, respectively. In Figure 5d, the pore-size distribution calculated by the Barrett–Joyner–Halenda (BJH) method indicates that the pores are mainly in the range of 2–10 nm. Compared with CS-

DOI: 10.1021/acsami.6b13153
ACS Appl. Mater. Interfaces 2017, 9, 3624–3633

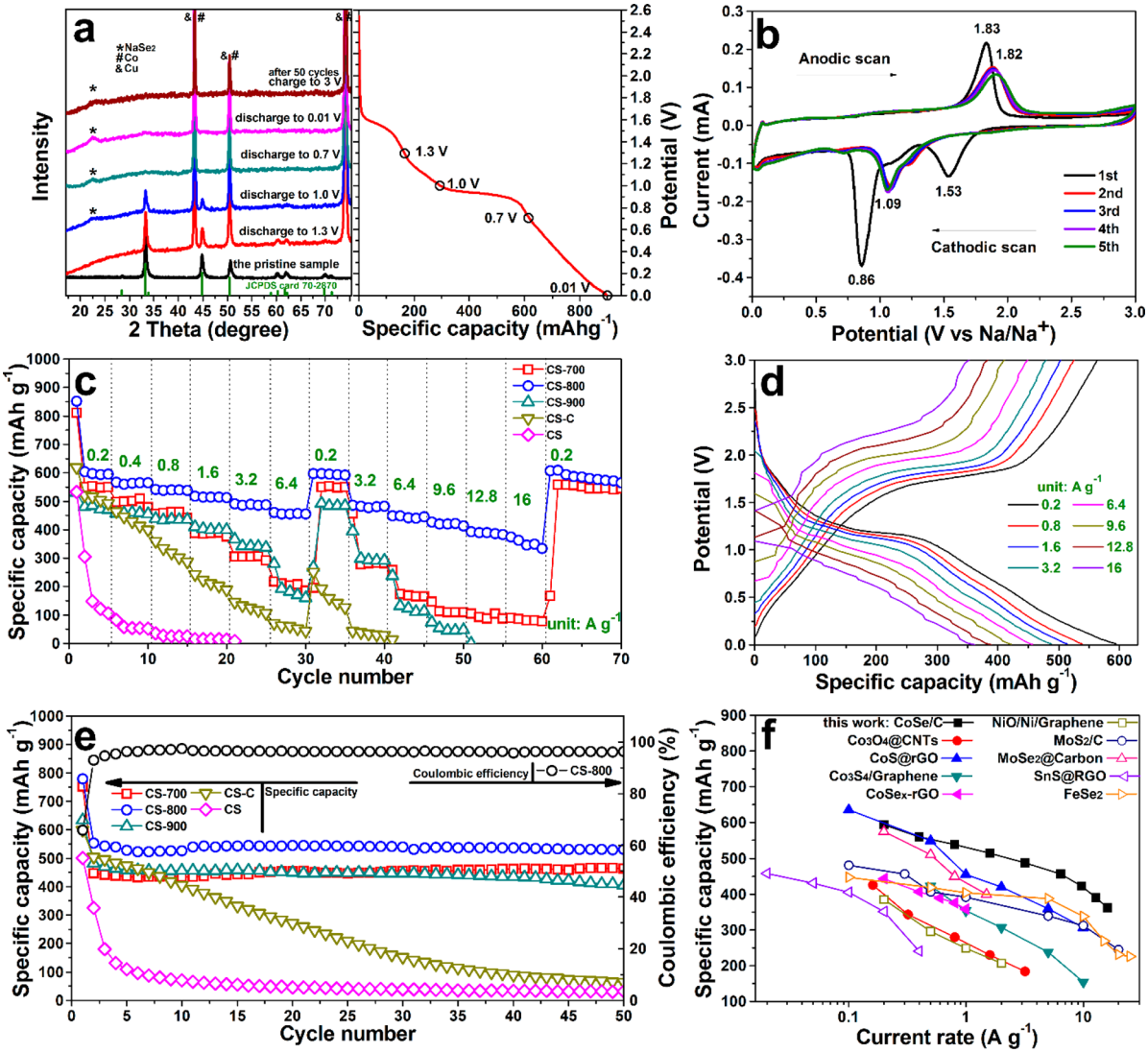

Figure 6. (a) Ex situ XRD patterns of the CS-800 electrode obtained at different charge−discharge stages at 200 mA g^{-1}. (b) The initial five successive CV curves of CS-800. (c) Rate capability of the nitrogen-doped CoSe/C, CoSe/C, and bare CoSe. (d) Charge−discharge curves at different current densities of CS-800. (e) The cycling performance of the electrodes at 500 mA g^{-1} between 0.01 and 3 V vs Na/Na^+. (f) The rate performances of the CS-800 electrode and many other anode materials for SIBs.

700 and CS-900, the CS-800 sample has the largest surface areas and most pores in the range of 2−10 nm. The incomplete carbonization of the organic species may lead to fewer mesopores in CS-700. As for CS-900, the abnormal growth of CoSe particles reduces the mesopores between the particles. The mesopores would provide the necessary pathway for electrolyte penetration and enlarge the contact area between electrode materials and electrolyte.

Novel cathode/anode materials are the key for high-performance sodium ion batteries.[43] In this work, the CoSe/C composites were assembled in half-cells to evaluate their sodium storage capability, and the electrochemical performances are shown in Figure 6. In order to investigate the reaction between Na and CoSe/C composite, an ex situ XRD experiment was carried out to study the phase transition among the discharge/charge process. Figure 6a shows the discharge profile and the corresponding ex situ XRD results of CS-800. In the discharge profile, the electrode exhibits a slight plateau at around 1.5 V and a large discharge plateau at around 0.8 V. According to previously reported CoS, $CoSe_x$, and other TMCs anodes materials for sodium ion batteries (SIBs), the plateaus may originate from the initial insertion of sodium to form the Na_xCoSe intermediate phase[5,44] and the subsequent displacement reaction for the formation of Na_2Se and Co:[18,44,45] $CoSe + xNa^+ + xe^- \rightarrow Na_xCoSe$; $Na_xCoSe + (2 - x)Na^+ + (2 - x)e^- \rightarrow Co + Na_2Se$. According to the ex situ XRD examination results (Figure 6a), CoSe phase is detected before the electrode is discharged to 1 V, indicating that the initial insertion of sodium ions does not cause a phase transition. The intermediate Na_xCoSe phase is not detected because of its low crystallinity.[44] When the electrode is discharged to 0.7 V and further to 0.01 V, no CoSe phase can be detected, but a minor diffraction peak of $NaSe_2$ is. The minor diffraction peaks imply that the electrochemical reaction products are in low crystallinity or amorphous. In Figure S8 (SI), the ex situ XRD patterns in the 2θ range between 73.3° and 74.9° at different discharge/charge states are shown. In the first discharge process, a CoC_x peak [JCPDS Card No. 44-0962: $P\bar{4}3m$ (No. 215), a = 3.6061 Å] becomes more obvious with deeper discharge, implying the gradual formation of CoC_x,

DOI: 10.1021/acsami.6b13153
ACS Appl. Mater. Interfaces 2017, 9, 3624−3633

which can be attributed to the dissolving of ZIF-67-derived carbon at high temperature during the synthesis process.[46] Similar to the reaction of transition-metal sulfides, the CoSe react with sodium ions through a conversion reaction, forming cobalt nanocrystals dispersed in the Na_2Se matrix.[44] Figure 6b shows the first five successive CV curves of CS-800 electrode between 0.01 and 3 V vs Na/Na^+ at a scan rate of 0.1 mV s^{-1}. For the first cycle, the detection of two cathodic peaks at 1.53 and 0.86 V indicates the multistep electrochemical reaction. These results corroborate well the discharge profile. The anodic peak at 1.83 V is due to the Na^+ ions removal process, along with the recovery of Na_xCoSe intermediate phase from metallic Co and Na_2Se.[18] After the first cycle, the cathodic peak intensity decreases significantly, and the peak shifts to 1.09 V vs Na/Na^+. The composite electrode shows large irreversible capability loss for the initial cycle, which can be attributed to the irreversible phase transition and the decomposition of electrolyte to form the solid electrolyte interface (SEI) layer on the electrode materials.[47] No obvious current decay is detected for the later cycles, indicating the improved reversibility of the electrode materials.

Figure 6c shows the rate capability of the nitrogen-doped CoSe/C composites. For comparison, bare CoSe particles (CS) and CoSe/C composite without nitrogen doping (CS-C) were also assembled into coin cells to study their electrochemical performances. The successful fabrication of CS and CS-C can be confirmed by XRD and Raman tests in Figure S9a,b (SI). The CS and CS-C are both composed of microparticles (Figure S9c,d, SI). As shown in Figure 6c, for CS-800, specific capacities of 594.1, 560.4, 538.2, 513.5, 487.6, 456.6, 422.2, 389.9, and 361.9 mA h g^{-1} can be achieved at the current densities of 0.2, 0.4, 0.8, 1.6, 3.2, 6.4, 9.6, 12.8, and 16 A g^{-1}, respectively. When the current is reset to 0.2 A g^{-1}, the electrode can recover its capacities, indicating the good rate capability. The capacity is calculated on the basis of the total mass of the CoSe/C composite. The CS-700 sample shows lower capacity, which may be owing to its higher carbon content. Moreover, the carbon framework of CS-700 is less graphitized, which results in lower electron transportation for the redox reactions than that in CS-800. For CS-900, although the electron transportation can be improved by the higher graphitization degree of carbon, the diffusion of sodium ions is reduced due to the larger particle size. For the CS-C and CS electrodes, which do not use the MOF as sacrificial templates, their rate performances are much worse. Almost no capacity can be detected for the CS electrode at the current density of 1.6 A g^{-1}. Figure 6d shows the charge−discharge curves of CS-800 electrode at different rates. The plateaus can be observed for all the charge−discharge profiles at different current densities, and the voltage gap between discharge and charge plateaus increases slightly with higher rate. The result also indicates the good rate ability of the electrode. Figure 6e shows the cycling performances of the electrodes at the current density of 500 mA g^{-1} between 0.01 and 3 V vs Na/Na^+. The nitrogen-doped CoSe/C samples exhibit much better cycling stability than the CS-C and CS electrodes. The result demonstrates that constructing CoSe nanoparticles within the nitrogen-doped carbon frameworks can indeed improve the cyclic stability. The CS-800 electrode can deliver a stabilized specific capacity of 552.5 mA h g^{-1} at the second cycle and retain 531.6 mA h g^{-1} after 50 cycles. The average capacity fading rate is 0.08% per cycle. The Coulombic efficiency is around 97% after five cycles, which may be owing to the side reactions and gradual decomposition of electrolyte. As can be seen in the ex situ XRD patterns in Figure S8 (SI), after 50 cycles and charging the electrode to 3 V, an obvious CoC_x peak can be observed. Moreover, the carbonate-based electrolytes can react with the intermediate products of transition-metal sulfides and selenides,[5,48] which may lead to the relative lower Coulombic efficiency. The SEM, TEM, and EDS results of the CS-800 electrodes after 50 cycles are given in Figure S10 (SI). Dodecahedra with a size of around 500 nm can still be distinguished in the SEM image of Figure S10a (SI). Although the primary particles for constructing the dodecahedron are bigger than the pristine sample in the TEM image of Figure S10b, the yolk−shell structure is reserved. The good structural reservation of the particles can be attributed to the good stability of the carbon skeleton. The larger particles may originate from the large volume expansion of active materials during the sodium uptake process and the gradual formation of SEI layers on the active materials. The EDS analysis reveal the existence of C, O, Co, Se, and Na elements, further implying the formation of the SEI layer. The cycling performance of 200 cycles at 2 A g^{-1} for CS-800 is given in Figure S11 (SI). The specific capacity of the electrode materials is very stable for the initial 60 cycles. However, the capacity starts to degrade thereafter. According to previous reports, the carbonate-based electrolytes may react with the intermediate products of CoSe,[5,48] which may lead to the decreased capacity. Among the nitrogen-doped CoSe/C electrodes, CS-800 shows the best electrochemical performance, which can be attributed to its relatively smaller particle size, highly graphitized carbon, higher content of nitrogen doping, and larger specific area. Figure 6f compares the rate capabilities of the CS-800 electrode and other electrodes for sodium ion batteries, from which we can tell that the rate capability of the nitrogen-doped, yolk−shell-structured CoSe/C mesoporous composite is superior to many reported anode materials for SIBs (Co_3O_4@CNTs,[49] CoS@rGO,[44] Co_3S_4/graphene,[50] $CoSe_x$−rGO,[18] NiO/Ni/graphene,[51] MoS_2/C,[52] $MoSe_2$@carbon,[53] SnS@RGO,[54] and $FeSe_2$[5]).

Electrochemical impedance spectroscopy (EIS) measurements were further employed to study the differences of the electrodes' performances. As shown in Figure S12 (SI), all the Nyquist plots are composed of a semicircle in the high-frequency region and a straight line in the low-frequency region. The semicircle is mainly ascribed to the charge-transfer reaction at the electrode/electrolyte interface. The slanted line in the low-frequency region is attributed to the diffusion process of sodium ions in the bulk of the electrode material.[55] The EIS results are fitted using an equivalent circuit shown in inset of Figure S12b (SI).[56] The simulated data are given in Table S1 (SI). The charge-transfer resistances (R_{ct}) of the nitrogen-doped CoSe/C electrodes are much smaller than that of the CoSe/C or bare CoSe electrode, suggesting that the nitrogen-doped carbon frameworks can effectively enhance the kinetics of electronic transportation in the electrode. Besides, the R_{ct} of the CS-800 electrode is 390.8 Ω, which is smaller than those of the other nitrogen-doped CoSe/C electrodes. The CS-800 electrode has relatively smaller particle size, and its carbon framework has a relatively higher extent of graphitization and more nitrogen doping. These advantages lead to its best electrochemical performances, including the superior rate capability and cycling stability.

On the basis of the above discussion, the superior electrochemical performances of the nitrogen-doped CoSe/C

DOI: 10.1021/acsami.6b13153
ACS Appl. Mater. Interfaces 2017, 9, 3624−3633

composites as electrode materials for SIBs can be attributed to the following issues: (1) the good contact between CoSe nanoparticles and carbon in the composite can ensure the good structural stability and electron conductivity; (2) the high level of nitrogen-doping can further improve the conductivity of the carbon skeleton; (3) the mesoporous yolk−shell structures of the composite can provide the space buffer upon electrochemical cycling for sodium ion insertion/deinsertion; and (4) the porous structure can provide an easy electrolyte penetration pathway and enlarge the contact area between electrode materials and electrolyte.

4. CONCLUSION

Nitrogen-doped, yolk−shell-structured CoSe/C mesoporous dodecahedra were prepared using cobalt-based organic frameworks as sacrificial templates. The CoSe nanoparticles are in situ formed in the nitrogen-doped carbon matrix by reacting ZIF-67 with selenium powders at different temperatures between 700 and 900 °C. With the temperature increasing, the carbon in the composite has a higher degree of graphitization. However, the content of nitrogen in the carbon decreases and the particle size of CoSe increases. For the CoSe/C composites synthesized at 800 °C, the carbon framework has a relatively higher extent of graphitization, with high nitrogen doping content (17.65%). Meanwhile, the CoSe nanoparticles, with size of around 15 nm, are coherently confined in the mesoporous carbon framework. Furthermore, the yolk−shell-structured mesoporous framework can facilitate the easy electrolyte penetration and volume changes. As electrode materials for sodium ion batteries, the CoSe/C dodecahedra exhibit excellent rate capability and cycling stability. The synthetic method may also be applicable to fabricate other transition-metal chalcogenides with high electrochemical performances.

ASSOCIATED CONTENT

Supporting Information

The Supporting Information is available free of charge on the ACS Publications website at DOI: 10.1021/acsami.6b13153.

XRD patterns and SEM images of ZIF-67; TG and DSC curves, high-resolution XPS spectra, XRD patterns, Raman spectra, and SEM images of CS or CoSe/C samples; XRD patterns, SEM image, TEM image, and EDS results of the electrode after cycles; Nyquist plots and fitting parameters; the detailed calculation method for the mass ratios of C, N, and CoSe in the composite (PDF)

AUTHOR INFORMATION

Corresponding Authors

*A.P. e-mail: pananqiang@csu.edu.cn.
*S.L. e-mail: lsq@csu.edu.cn.
*G.C. e-mail: gzcao@u.washington.edu.

ORCID

Anqiang Pan: 0000-0002-7605-1192
Guozhong Cao: 0000-0003-1498-4517

Notes

The authors declare no competing financial interest.

ACKNOWLEDGMENTS

This work was supported by the National Natural Science Foundation of China (Grant Nos. 51302323, 51374255, and 51322403), the Program for New Century Excellent Talents in University (Grant No. NCET-13-0594), the Research Fund for the Doctoral Program of Higher Education of China (Grant No. 201301621200), the Natural Science Foundation of Hunan Province, China (Grant No. 14JJ3018), and the Fundamental Research Funds for the Central Universities of Central South University (Grant No. 2016zzts026).

REFERENCES

(1) Dunn, B.; Kamath, H.; Tarascon, J.-M. Electrical Energy Storage for the Grid: A Battery of Choices. *Science* **2011**, *334* (6058), 928−935.

(2) Yang, Z.; Zhang, J.; Kintner-Meyer, M. C. W.; Lu, X.; Choi, D.; Lemmon, J. P.; Liu, J. Electrochemical Energy Storage for Green Grid. *Chem. Rev.* **2011**, *111* (5), 3577−3613.

(3) Liu, C.; Li, F.; Ma, L.-P.; Cheng, H.-M. Advanced Materials for Energy Storage. *Adv. Mater.* **2010**, *22* (8), E28−E62.

(4) Wang, Q.; Zou, R.; Xia, W.; Ma, J.; Qiu, B.; Mahmood, A.; Zhao, R.; Yang, Y.; Xia, D.; Xu, Q. Facile Synthesis of Ultrasmall CoS_2 Nanoparticles within Thin N-Doped Porous Carbon Shell for High Performance Lithium-Ion Batteries. *Small* **2015**, *11* (21), 2511−2517.

(5) Zhang, K.; Hu, Z.; Liu, X.; Tao, Z.; Chen, J. $FeSe_2$ Microspheres as a High-Performance Anode Material for Na-Ion Batteries. *Adv. Mater.* **2015**, *27* (21), 3305−3309.

(6) Zhang, Y.; Pan, A.; Wang, Y.; Wei, W.; Su, Y.; Hu, J.; Cao, G.; Liang, S. Dodecahedron-Shaped Porous Vanadium Oxide and Carbon Composite for High-Rate Lithium Ion Batteries. *ACS Appl. Mater. Interfaces* **2016**, *8* (27), 17303−17311.

(7) Lin, J.; Peng, Z.; Xiang, C.; Ruan, G.; Yan, Z.; Natelson, D.; Tour, J. M. Graphene Nanoribbon and Nanostructured SnO_2 Composite Anodes for Lithium Ion Batteries. *ACS Nano* **2013**, *7* (7), 6001−6006.

(8) Yu, G.; Xie, X.; Pan, L.; Bao, Z.; Cui, Y. Hybrid Nanostructured Materials for High-Performance Electrochemical Capacitors. *Nano Energy* **2013**, *2* (2), 213−234.

(9) Zhang, W.-M.; Wu, X.-L.; Hu, J.-S.; Guo, Y.-G.; Wan, L.-J. Carbon Coated Fe_3O_4 Nanospindles as a Superior Anode Material for Lithium-Ion Batteries. *Adv. Funct. Mater.* **2008**, *18* (24), 3941−3946.

(10) Gu, D.; Li, W.; Wang, F.; Bongard, H.; Spliethoff, B.; Schmidt, W.; Weidenthaler, C.; Xia, Y.; Zhao, D.; Schueth, F. Controllable Synthesis of Mesoporous Peapod-like Co_3O_4@Carbon Nanotube Arrays for High-Performance Lithium-Ion Batteries. *Angew. Chem., Int. Ed.* **2015**, *54* (24), 7060−7064.

(11) Sun, H.; Sun, X.; Hu, T.; Yu, M.; Lu, F.; Lian, J. Graphene-Wrapped Mesoporous Cobalt Oxide Hollow Spheres Anode for High-Rate and Long-Life Lithium Ion Batteries. *J. Phys. Chem. C* **2014**, *118* (5), 2263−2272.

(12) Pan, A.; Wu, H. B.; Yu, L.; Lou, X. W. Template-Free Synthesis of VO_2 Hollow Microspheres with Various Interiors and Their Conversion into V_2O_5 for Lithium-Ion Batteries. *Angew. Chem., Int. Ed.* **2013**, *52* (8), 2226−2230.

(13) Wang, J.; Zhang, X.; Wei, Q.; Lv, H.; Tian, Y.; Tong, Z.; Liu, X.; Hao, J.; Qu, H.; Zhao, J.; Li, Y.; Mai, L. 3D Self-Supported Nanopine Forest-Like Co_3O_4@$CoMoO_4$ Core-Shell Architectures for High-Energy Solid State Supercapacitors. *Nano Energy* **2016**, *19*, 222−233.

(14) Yue, J. L.; Sun, Q.; Fu, Z. W. Cu_2Se with Facile Synthesis as a Cathode Material for Rechargeable Sodium Batteries. *Chem. Commun. (Cambridge, U. K.)* **2013**, *49* (52), 5868−5870.

(15) Tan, C.; Zhang, H. Two-Dimensional Transition Metal Dichalcogenide Nanosheet-Based Composites. *Chem. Soc. Rev.* **2015**, *44* (9), 2713−2731.

(16) Zhang, L.-f.; Zhang, C.-y. Multifunctional $Co_{0.85}Se$/Graphene Hybrid Nanosheets: Controlled Synthesis and Enhanced Performances for the Oxygen Reduction Reaction and Decomposition of Hydrazine Hydratet. *Nanoscale* **2014**, *6* (3), 1782−1789.

DOI: 10.1021/acsami.6b13153
ACS Appl. Mater. Interfaces 2017, 9, 3624−3633

(17) Li, Z.; Xue, H.; Wang, J.; Tang, Y.; Lee, C.-S.; Yang, S. Reduced Graphene Oxide/Marcasite-Type Cobalt Selenide Nanocrystals as an Anode for Lithium-Ion Batteries with Excellent Cyclic Performance. *ChemElectroChem* **2015**, *2* (11), 1682−1686.
(18) Park, G. D.; Kang, Y. C. One-Pot Synthesis of $CoSe_x$-rGO Composite Powders by Spray Pyrolysis and Their Application as Anode Material for Sodium-Ion Batteries. *Chem. - Eur. J.* **2016**, *22* (12), 4140−4146.
(19) Banerjee, A.; Bhatnagar, S.; Upadhyay, K. K.; Yadav, P.; Ogale, S. Hollow $Co_{0.85}Se$ Nanowire Array on Carbon Fiber Paper for High Rate Pseudocapacitor. *ACS Appl. Mater. Interfaces* **2014**, *6* (21), 18844−18852.
(20) Yu, N.; Zhu, M.-Q.; Chen, D. Flexible All-Solid-State Asymmetric Supercapacitors with Three-Dimensional $CoSe_2$/Carbon Cloth Electrodes. *J. Mater. Chem. A* **2015**, *3* (15), 7910−7918.
(21) Tang, J.; Salunkhe, R. R.; Liu, J.; Torad, N. L.; Imura, M.; Furukawa, S.; Yamauchi, Y. Thermal Conversion of Core-Shell Metal-Organic Frameworks: A New Method for Selectively Functionalized Nanoporous Hybrid Carbon. *J. Am. Chem. Soc.* **2015**, *137* (4), 1572−1580.
(22) Torad, N. L.; Salunkhe, R. R.; Li, Y. Q.; Hamoudi, H.; Imura, M.; Sakka, Y.; Hu, C. C.; Yamauchi, Y. Electric Double-Layer Capacitors Based on Highly Graphitized Nanoporous Carbons Derived from ZIF-67. *Chem. - Eur. J.* **2014**, *20* (26), 7895−7900.
(23) Zhong, S.; Zhan, C. X.; Cao, D. P. Zeolitic Imidazolate Framework-Derived Nitrogen-Doped Porous Carbons as High Performance Supercapacitor Electrode Materials. *Carbon* **2015**, *85*, 51−59.
(24) Gueon, D.; Moon, J. H. Nitrogen-Doped Carbon Nanotube Spherical Particles for Supercapacitor Applications: Emulsion-Assisted Compact Packing and Capacitance Enhancement. *ACS Appl. Mater. Interfaces* **2015**, *7* (36), 20083−20089.
(25) Shen, W.; Wang, C.; Xu, Q. J.; Liu, H. M.; Wang, Y. G. Nitrogen-Doping-Induced Defects of a Carbon Coating Layer Facilitate Na-Storage in Electrode Materials. *Adv. Energy Mater.* **2015**, *5* (1), 1400982.
(26) Wang, L.; Wu, J.; Chen, Y.; Wang, X.; Zhou, R.; Chen, S.; Guo, Q.; Hou, H.; Song, Y. Hollow Nitrogen-doped Fe_3O_4/Carbon Nanocages with Hierarchical Porosities as Anode Materials for Lithium-ion Batteries. *Electrochim. Acta* **2015**, *186*, 50−57.
(27) Wang, H.; Zhang, C.; Liu, Z.; Wang, L.; Han, P.; Xu, H.; Zhang, K.; Dong, S.; Yao, J.; Cui, G. Nitrogen-Doped Graphene Nanosheets with Excellent Lithium Storage Properties. *J. Mater. Chem.* **2011**, *21* (14), 5430−5434.
(28) Chen, T.; Hu, Y.; Cheng, B.; Chen, R.; Lv, H.; Ma, L.; Zhu, G.; Wang, Y.; Yan, C.; Tie, Z.; Jin, Z.; Liu, J. Multi-Yolk-Shell Copper Oxide@Carbon Octahedra as High-Stability Anodes for Lithium-Ion Batteries. *Nano Energy* **2016**, *20*, 305−314.
(29) Wu, R.; Wang, D. P.; Rui, X.; Liu, B.; Zhou, K.; Law, A. W.; Yan, Q.; Wei, J.; Chen, Z. In-Situ Formation of Hollow Hybrids Composed of Cobalt Sulfides Embedded within Porous Carbon Polyhedra/Carbon Nanotubes for High-Performance Lithium-Ion Batteries. *Adv. Mater.* **2015**, *27* (19), 3038−3044.
(30) Yin, W.; Shen, Y.; Zou, F.; Hu, X. L.; Chi, B.; Huang, Y. H. Metal-Organic Framework Derived ZnO/$ZnFe_2O_4$/C Nanocages as Stable Cathode Material for Reversible Lithium-Oxygen Batteries. *ACS Appl. Mater. Interfaces* **2015**, *7* (8), 4947−4954.
(31) Guo, Y.; Yu, L.; Wang, C.-Y.; Lin, Z.; Lou, X. W. Hierarchical Tubular Structures Composed of Mn-Based Mixed Metal Oxide Nanoflakes with Enhanced Electrochemical Properties. *Adv. Funct. Mater.* **2015**, *25* (32), 5184−5189.
(32) Lai, Y. Q.; Gan, Y. Q.; Zhang, Z. A.; Chen, W.; Li, J. Metal-Organic Frameworks-Derived Mesoporous Carbon for High Performance Lithium-Selenium Battery. *Electrochim. Acta* **2014**, *146*, 134−141.
(33) Campos, C. E. M.; de Lima, J. C.; Grandi, T. A.; Machado, K. D.; Pizani, P. S. Structural Studies of Cobalt Selenides Prepared by Mechanical Alloying. *Phys. B* **2002**, *324* (1−4), 409−418.
(34) Wang, X. J.; Zhou, J. W.; Fu, H.; Li, W.; Fan, X. X.; Xin, G. B.; Zheng, J.; Li, X. G. MOF Derived Catalysts for Electrochemical Oxygen Reduction. *J. Mater. Chem. A* **2014**, *2* (34), 14064−14070.
(35) Qiu, W.; Jiao, J.; Xia, J.; Zhong, H.; Chen, L. A Self-Standing and Flexible Electrode of Yolk-Shell CoS_2 Spheres Encapsulated with Nitrogen-Doped Graphene for High-Performance Lithium-Ion Batteries. *Chem. - Eur. J.* **2015**, *21* (11), 4359−4367.
(36) Xia, W.; Zhu, J. H.; Guo, W. H.; An, L.; Xia, D. G.; Zou, R. Q. Well-Defined Carbon Polyhedrons Prepared from Nano Metal-Organic Frameworks for Oxygen Reduction. *J. Mater. Chem. A* **2014**, *2* (30), 11606−11613.
(37) Zhang, C. H.; Fu, L.; Liu, N.; Liu, M. H.; Wang, Y. Y.; Liu, Z. F. Synthesis of Nitrogen-Doped Graphene Using Embedded Carbon and Nitrogen Sources. *Adv. Mater.* **2011**, *23* (8), 1020−1024.
(38) Zhao, J.; Lai, H. W.; Lyu, Z. Y.; Jiang, Y. F.; Xie, K.; Wang, X. Z.; Wu, Q.; Yang, L. J.; Jin, Z.; Ma, Y. W.; Liu, J.; Hu, Z. Hydrophilic Hierarchical Nitrogen-Doped Carbon Nanocages for Ultrahigh Supercapacitive Performance. *Adv. Mater.* **2015**, *27* (23), 3541−3545.
(39) Sui, Z. Y.; Meng, Y. N.; Xiao, P. W.; Zhao, Z. Q.; Wei, Z. X.; Han, B. H. Nitrogen-Doped Graphene Aerogels as Efficient Supercapacitor Electrodes and Gas Adsorbents. *ACS Appl. Mater. Interfaces* **2015**, *7* (3), 1431−1438.
(40) Qie, L.; Chen, W. M.; Wang, Z. H.; Shao, Q. G.; Li, X.; Yuan, L. X.; Hu, X. L.; Zhang, W. X.; Huang, Y. H. Nitrogen-Doped Porous Carbon Nanofiber Webs as Anodes for Lithium Ion Batteries with a Superhigh Capacity and Rate Capability. *Adv. Mater.* **2012**, *24* (15), 2047−2050.
(41) Zheng, F.; Yang, Y.; Chen, Q. High Lithium Anodic Performance of Highly Nitrogen-Doped Porous Carbon Prepared from a Metal-Organic Framework. *Nat. Commun.* **2014**, *5*, 5261.
(42) Sing, K. S. W. Reporting Physisorption Data for Gas/Solid Systems with Special Reference to the Determination of Surface Area and Porosity. *Pure Appl. Chem.* **1985**, *57*, 603−619.
(43) Masse, R. C.; Uchaker, E.; Cao, G. Z. Beyond Li-Ion: Electrode Materials for Sodium- and Magnesium-Ion Batteries. *Science China-Materials* **2015**, *58* (9), 715−766.
(44) Peng, S.; Han, X.; Li, L.; Zhu, Z.; Cheng, F.; Srinivansan, M. U.; Adams, S.; Ramakrishna, S. Unique Cobalt Sulfide/Reduced Graphene Oxide Composite as an Anode for Sodium-Ion Batteries with Superior Rate Capability and Long Cycling Stability. *Small* **2016**, *12* (10), 1359−1368.
(45) Zhou, Q.; Liu, L.; Guo, G.; Yan, Z.; Tan, J.; Huang, Z.; Chen, X.; Wang, X. Sandwich-Like Cobalt Sulfide-Graphene Composite - an Anode Material with Excellent Electrochemical Performance for Sodium Ion Batteries. *RSC Adv.* **2015**, *5* (88), 71644−71651.
(46) Chen, L.; Mashimo, T.; Iwamoto, C.; Okudera, H.; Omurzak, E.; Ganapathy, H. S.; Ihara, H.; Zhang, J.; Abdullaeva, Z.; Takebe, S.; Yoshiasa, A. Synthesis of Novel CoC_x@C Nanoparticles. *Nanotechnology* **2013**, *24* (4), 045602.
(47) Zhang, Z.; Yang, X.; Fu, Y.; Du, K. Ultrathin Molybdenum Diselenide Nanosheets Anchored on Multi-Walled Carbon Nanotubes as Anode Composites for High Performance Sodium-Ion Batteries. *J. Power Sources* **2015**, *296*, 2−9.
(48) Hu, Z.; Zhu, Z.; Cheng, F.; Zhang, K.; Wang, J.; Chen, C.; Chen, J. Pyrite FeS_2 for High-Rate and Long-Life Rechargeable Sodium Batteries. *Energy Environ. Sci.* **2015**, *8* (4), 1309−1316.
(49) Jian, Z.; Liu, P.; Li, F.; Chen, M.; Zhou, H. Monodispersed Hierarchical Co_3O_4 Spheres Intertwined with Carbon Nanotubes for Use as Anode Materials in Sodium-Ion Batteries. *J. Mater. Chem. A* **2014**, *2* (34), 13805−13809.
(50) Du, Y.; Zhu, X.; Zhou, X.; Hu, L.; Dai, Z.; Bao, J. Co_3S_4 Porous Nanosheets Embedded in Graphene Sheets as High-Performance Anode Materials for Lithium and Sodium Storage. *J. Mater. Chem. A* **2015**, *3* (13), 6787−6791.
(51) Zou, F.; Chen, Y.-M.; Liu, K.; Yu, Z.; Liang, W.; Bhaway, S. M.; Gao, M.; Zhu, Y. Metal Organic Frameworks Derived Hierarchical Hollow NiO/Ni/Graphene Composites for Lithium and Sodium Storage. *ACS Nano* **2016**, *10* (1), 377−386.

DOI: 10.1021/acsami.6b13153
ACS Appl. Mater. Interfaces 2017, 9, 3624−3633

(52) Lu, Y.; Zhao, Q.; Zhang, N.; Lei, K.; Li, F.; Chen, J. Facile Spraying Synthesis and High-Performance Sodium Storage of Mesoporous MoS_2/C Microspheres. *Adv. Funct. Mater.* **2016**, *26* (6), 911−918.
(53) Yang, X.; Zhang, Z.; Fu, Y.; Li, Q. Porous Hollow Carbon Spheres Decorated with Molybdenum Diselenide Nanosheets as Anodes for Highly Reversible Lithium and Sodium Storage. *Nanoscale* **2015**, 7 (22), 10198−10203.
(54) Wu, L.; Lu, H.; Xiao, L.; Ai, X.; Yang, H.; Cao, Y. Improved Sodium-Storage Performance of Stannous Sulfide@Reduced Graphene Oxide Composite as High Capacity Anodes for Sodium-Ion Batteries. *J. Power Sources* **2015**, *293*, 784−789.
(55) Rui, X.; Sun, W.; Wu, C.; Yu, Y.; Yan, Q. An Advanced Sodium-Ion Battery Composed of Carbon Coated $Na_3V_2(PO_4)_3$ in a Porous Graphene Network. *Adv. Mater.* **2015**, *27* (42), 6670−6676.
(56) Liang, S.; Cao, X.; Wang, Y.; Hu, Y.; Pan, A.; Cao, G. Uniform $8LiFePO_4 \bullet Li_3V_2(PO_4)_3$/C Nanoflakes for High-Performance Li-Ion Batteries. *Nano Energy* **2016**, *22*, 48−58.

DOI: 10.1021/acsami.6b13153
ACS Appl. Mater. Interfaces 2017, 9, 3624−3633